Magnetically Active GO-Fe_3O_4 Nanocomposite for Enhanced Rhodamine B Removal Efficiency

Alexander Souhuat, Henry Fonda Aritonang*, and Harry Steven Julius Koleangan

Department of Chemistry, Faculty of Mathematics and Natural Sciences, Sam Ratulangi University, Jl. Kampus Unsrat Kleak, Manado 95115, Indonesia

** Corresponding author:*

tel: +62-8124450362
email: henryaritonang@unsrat.ac.id

Received: May 22, 2024
Accepted: August 23, 2024

DOI: 10.22146/ijc.96383

Abstract: *According to the World Bank study, approximately 17–20% of water contamination is attributed to the textile industry. The quantity of waste produced increases as a result of increased productivity. Textile wastewater contains dyes such as rhodamine B (RhB), which are hazardous and challenging to remove using standard methods. Adsorption utilizing nano-adsorbents has been widely researched and developed to remove dyes from the environment because of its numerous advantages. Graphene oxide-magnetite (GO-Fe_3O_4) has been extensively explored as an adsorbent due to its large surface area, strong bonding, and ease of separation from water. In this study, GO-Fe_3O_4 was synthesized by combining GO from coconut shell with Fe_3O_4 from iron sand as an absorbent to lower the amount of RhB. Various analytical techniques, including XRD, SEM-EDS, TEM, FTIR, and UV-vis, were employed to examine the properties of the composites. The GO-Fe_3O_4 exhibited a maximum adsorption capacity of 34.590 mg/g under specific conditions, i.e., 0.5 g adsorbent dosage, pH 4, and a 2 h contact time. The adsorption followed the pseudo-second-order kinetics model with 0.00016 mg/g min adsorption rate while the adsorption isotherm followed the Langmuir model where adsorbent surfaces are spread homogeneously by forming a monolayer.*

Keywords: *adsorption; coconut shell; graphene oxide-Fe_3O_4; nano-adsorbent; rhodamine B*

■ INTRODUCTION

The textile, paper, tanning, and printing sectors frequently employ dyes in their industrial processes. China is the world leader in textile production and exports. Based on China's yearly ecological environment data, textile effluent in the country amounted to roughly 184 million tons in 2021 [1]. The dyeing and finishing processes account for approximately 80% of the wastewater and contaminants produced by the entire textile industry [2]. The complex aromatic molecular structures of dyes render them highly stable and resistant to biodegradation. Moreover, many dyes are toxic and carcinogenic [3-4]. One of the most commonly used synthetic dyes is rhodamine B (RhB), which, when present in excessive amounts in the environment, can raise the pH of the water, thus affecting microorganisms, plants, and animals. RhB can enter the human body through the food chain, and excessive intake can cause liver and kidney degeneration, skin irritation, pulmonary inflammation, hemolysis, and comparable conditions when it surpasses the highest permissible level (tolerance threshold) of 140 μg/L [5-9]. Currently, the methods for dealing with RhB waste include membrane filtration [10], electroplating [11], adsorption [12], and coagulation [13]. Among these methods, the adsorption method is considered superior owing to its flexibility, abundant resources, low cost, ease of performance, and non-toxic final product [14]. In recent years, there has been a significant increase in research on RhB adsorption using various adsorbents. Some adsorbents, such as zeolites, activated charcoal, and magnetite can be used, however, the adsorption process is less effective and leads to the production of sludge, posing a new challenge [15].

Graphene oxide (GO) is a promising adsorbent due to its reusable nature, large surface area, and strong adsorption ability [16-18]. These properties were attributed to the existence of hydrophilic oxygen-containing functional groups and negatively charged surfaces in acidic environments. The modified Hummers method is the most effective approach for synthesizing GO [19]. The production of GO necessitates graphite derived from biomass waste, such as coconut shells. These shells exhibit exceptional characteristics, including being rich in carbon and serving as an eco-friendly solid fuel alternative to other biomass sources and coal materials [20]. GO can be combined with various materials, including Fe_3O_4.

Magnetic separation is a more convenient process when using superparamagnetic Fe_3O_4. This method has several advantages, such as its capacity to easily separate phases in aqueous solutions and its ability to treat large amounts of wastewater quickly, making it efficient and cost-effective. Consequently, numerous studies have been conducted on the synthesis of magnetic materials and their use for separation, with a particular emphasis on dye removal [15,21-22].

North Sulawesi is rich in coconut plantations and beaches containing iron sands. According to Directorate General of Estate Crops, 2022, Statistical of National Leading Estate Crops Commodity 2020-2022, coconut plantation products in North Sulawesi Province reached 270,515 tons [23]. North Sulawesi boasts several beaches, including Hais, Minanga, Lalow, and Lolan, which possess a considerable quantity of iron sand that can be transformed into magnetite [24-25]. This study examined the application of GO-Fe_3O_4 in removing RhB dye, contributing to the quest for environmentally friendly and secure alternative methods of water treatment.

■ EXPERIMENTAL SECTION

Materials

Coconut shells and iron sand were sourced from Tetey Village and Watuliney Village, respectively, both located in Southeast Sulawesi, Indonesia. The chemicals utilized in this study, such as hydrochloric acid (HCl, 37%), hydrogen peroxide (H_2O_2, 30%), sodium hydroxide (NaOH, 99.9%), sulfuric acid (H_2SO_4, 98%), nitric acid (HNO_3, 63%), ammonium hydroxide (NH_4OH, 25%), potassium permanganate ($KMnO_4$, 99.9%), and RhB ($C_{28}H_{31}ClN_2O_3$) were procured from Merck, Germany.

Instrumentation

The equipment used is glassware (Pyrex), 200 mesh sieve (KZM), filter paper (Whatman 42), herb grinder (FCT-Z100), magnetic stirrer (Witeg MS-20D), oven (Memmert UM 200), muffle furnace (SESW-1225), analytical scales (FA2204G), FTIR (Thermo Scientific Nicloet iS10), XRD (Beruder AXS D8 Advance ECO), SEM-EDS (JSM-6510LA), TEM (JEOL HT-7700), and UV-vis (Shimazu UV-1800).

Procedure

Iron sand preparation

The procedure of iron sand preparation was carried out using the acid treatment technique. Initially, the sample was washed with running water, and then heated at 100 °C for 24 h. After heating, it was crushed and sifted using a 200-mesh sieve. The iron sand powder was subsequently separated using a permanent magnet. An amount of 20 g of iron sand powder was combined with 70 mL of 37% HCl and agitated at 400 rpm for 60 min at 70 °C. The resulting solution was then filtered to obtain the liquid filtrate, which was subsequently utilized in subsequent synthesis processes.

Synthesis of graphite

The process of graphite synthesis was carried out using a previous method [26], which comprised several stages. Initially, the coconut shell was thoroughly cleaned and then crushed into a smaller size. The samples were placed in an oven and allowed to desiccate overnight at 50 °C. The dried coconut shells were ground into a fine powder using a grinder and sifted through a 200-mesh sieve. The sample was then carbonized at a temperature of 600 °C for 3 h to produce graphite, which was subsequently sifted through a 200-mesh sieve. The sifted graphite was added to 40% hydrofluoric acid in a ratio of 1:3 (w/v) and stirred at 45 °C for 3 h. Subsequently, the graphite underwent washing with a 0.1 M NaOH solution until the pH

reached a neutral level. It was then dried in an oven at 110 °C for 12 h.

Synthesis of GO

The synthesis of GO was carried out using a modified Hummer method [5]. Specifically, 3 g of graphite was combined with 70 mL of H_2SO_4 in a low temperature (10–15 °C) bath and stirred at 600 rpm for 30 min. Subsequently, 9 g of $KMnO_4$ was added to the solution, which was then transferred to an oil bath and stirred for 30 min at 45 °C. Following this, 150 L of aqueous was added to the solution and stirred for 15 min at 95 °C. Next, 500 mL of aqueous solution was added, followed by a dropwise addition of 15 mL of H_2O_2. The resulting solution was filtered and the precipitate was washed with 250 mL of 10% HCl. Finally, the characterization of the resulting GO was performed using SEM-EDS, FTIR, and XRD.

Synthesis of GO-Fe_3O_4

The synthesis of GO-Fe_3O_4 nanocomposites was achieved through the application of a modified method [27-28]. Initially, 0.2 g of GO was suspended in 200 mL of aqueous solution, which was subjected to sonication for 1 h to form a stable suspension. After that, 5 mL of iron sand filtrate was added to the suspension and sonicated for 30 min. Subsequently, 100 mL of 25% NH_4OH was added dropwise until the pH of the mixture reached 11–12. The solid product was obtained by stirring the mixture at 85 °C for 4 h and then filtration. The properties of the solid product were analyzed by FTIR, SEM-EDS, TEM, and XRD.

■ RESULTS AND DISCUSSION

Characterization

XRD analysis

The crystal structure of synthesized magnetic nanoparticles was evaluated using XRD analysis. XRD patterns were obtained for coconut shell powder (CSP), graphite, GO, GO-Fe_3O_4 nanocomposite and are shown in Fig. 1.

The predominant diffraction maxima observed for CSP are around 15.9, 21.9 and 34.6°, which represents cordierite ($Mg_2Al_4Si_5O_{18}$), quartz (SiO_2), and moissanite (SiC), respectively [29], with quartz having the high intensity. The diffraction occurring at 2θ of 22 and 44.5°

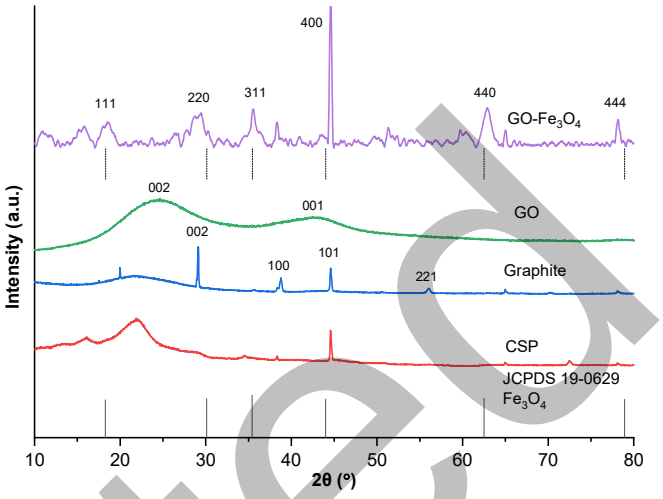

Fig 1. XRD pattern of JCPDS 19-0629, CSP, graphite, GO, and GO-Fe_3O_4

represents silicate minerals and sodalities, respectively [30]. Following the carbonization process, the CSP transformed into graphite. The graphite displayed peaks at 2θ values corresponding to the typical lattice planes of graphitic carbon, specifically (002), (100), (101), and (221), as indicated in the Joint Committee on Powder Diffraction Standards (JCPDS: 01-075-1621).

The graphite oxidation process has been observed to shift peaks at (002) and (001) to 24.67 and 43.24°, respectively, which suggests that the graphite has been fully oxidized into GO. The rise in peak positions can be ascribed to the intercalation of oxide functional groups, such as epoxy, hydroxyl, carbonyl, and carboxyl groups, at the carbon basal plane during the chemical oxidation reaction [26,31]. This intercalation leads to an expansion in the distance between consecutive carbon layers.

For the GO-Fe_3O_4 nanocomposites spectrum, this diffraction peak disappears, confirming that the stacking of GO sheets in the nanocomposite was almost disordered. The peaks of (111), (220), (331), (400), (440), and (444) for GO-Fe_3O_4, as well as the peak at 35.44°, align with the cubic inverse spinel structure of magnetite, according to the JCPDS: 00-19-0629. This result is consistent with the findings of Gautam's research [32]. According to the Debye–Scherrer' (Eq. (1)), the GO-Fe_3O_4 nanoparticles indicated the average crystalline size (d) of about 8.81 nm, which was calculated based on β as the width at half-maximum of the

main peak (311) refection at 2θ = 35.6°.

$$d = \frac{K\lambda}{\beta \cos\theta} \quad (1)$$

The parameters of this equation include K (0.9), λ (0.154 nm), and θ, which represent the constant, wavelength, and Bragg's angle, respectively.

FTIR analysis

The synthesized products were analyzed with FTIR, which investigates functional groups in CSP, graphite, GO, and GO-Fe_3O_4. FTIR spectrum of the CSP is shown in Fig. 2. From the gained result, the band shifting around the broad peak at 3347 cm^{-1} indicates the possible involvement of the O–H group. The peak at 2911 cm^{-1} is due to the C–H stretching that causes vibrations of CH, CH_2, and CH_3 groups. In 1732 cm^{-1}, the vibration of the group C=O appears. The absorption bands at about 1573 cm^{-1} show the characteristic of C=C aromatic rings. That can be seen in the increments in the C–O and bands at 1239 and 1079 cm^{-1}. The peak at 899 cm^{-1} is attributed to Si–O stretching and bending, indicating the presence of silica.

The FTIR spectra of graphite and graphene oxide are shown in Fig. 2. GO exhibits representative peaks at 3432, 1703, 1702, 1573, 1079 and 741 cm^{-1} corresponding vibration with the flexion of the O–H stretch, C=O stretch, aromatic C=C which did not oxidize, C–O stretch, C–H stretch, respectively. The FTIR spectrum of the GO sample accorded well with the previous works [33]. The

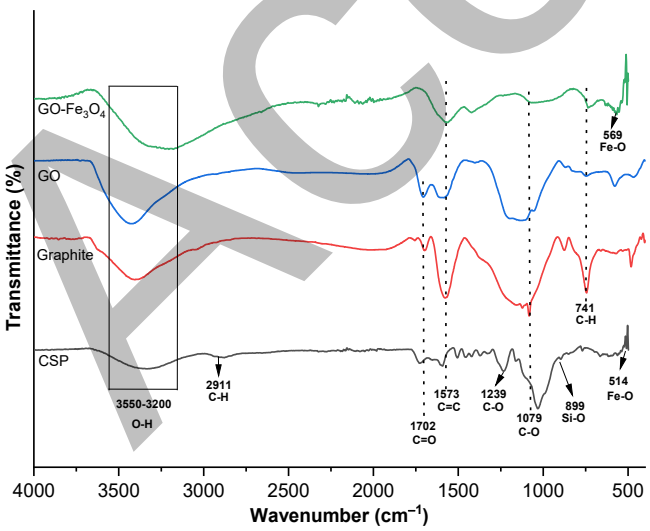

Fig 2. FTIR spectrum of CSP, graphite, GO, and GO-Fe_3O_4

FTIR spectrum of the GO-Fe_3O_4 nanocomposite reveals the presence of specific functional groups. At 1573 cm^{-1}, the vibration of C=C is detected, while peaks at 1073 and 1702 cm^{-1} correspond to the epoxy (C–O) and C=O groups, respectively. The degree of absorption at 3270 cm^{-1} indicates the existence of O–H groups, which suggests the formation of GO. Additionally, a new prominent absorption band appears at 569 cm^{-1} in the FTIR spectrum, corresponding to the stretching mode of Fe–O, as reported previously [13].

SEM-EDS analysis

The structural morphology and basic composition of samples CSP, graphite, GO, and GO-Fe_3O_4 were analyzed using SEM-EDS. The analysis results are shown in Fig. 3. The CSP micrograph in Fig. 3(a) shows a morphology in the form of clusters with a smooth surface. However, after going through the carbonization process and removing impurities, a three-dimensional structure with smaller size and pores has formed on the graphite micrograph in Fig. 3(b).

The morphology analysis of GO shown in Fig. 3(c) indicates a 2D structure with a smooth surface and various pore sizes ranging from meso-macro. On the other hand, the GO-Fe_3O_4 sample presents a porous texture that can be attributed to the rapid evaporation of the GO-Fe_3O_4 phase during the synthesis process. Additionally, small granular particles on the GO surface indicate that the Fe_3O_4 particles have adhered to the GO layer, indicating that the GO-Fe_3O_4 synthesis has been completed [11,17].

The EDS is shown in Fig. 4. The main components of GO are carbon and oxygen, with a carbon and oxygen atom ratio of 71.57 and 28.43. This suggests that the graphite oxidation process was successful in the presence of oxygenated functional groups in GO. The EDS analysis of the GO-Fe_3O_4 sample showed that magnetic nanoparticles were incorporated within the GO, with the dominant elements being carbon, oxygen, and iron, with an atomic ratio of 55.51, 10.40, and 34.09, respectively.

TEM analysis

The images in Fig. 5 provide a visual representation of the morphology of the GO-Fe_3O_4 composite material.

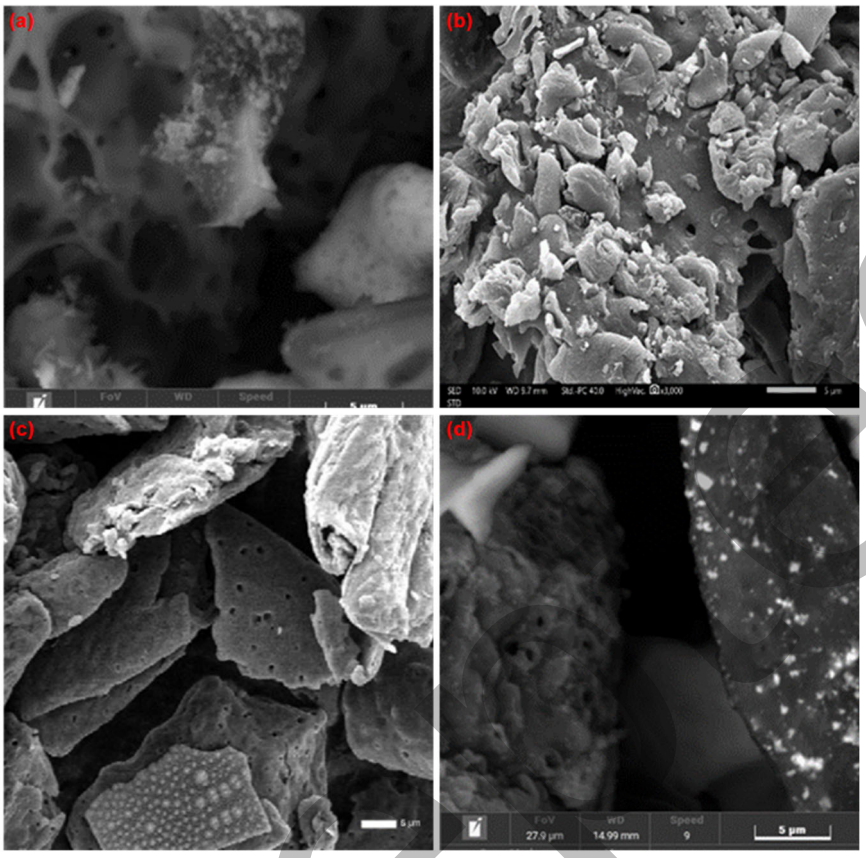

Fig 3. SEM images of (a) CSP, (b) graphite, (c) GO, and (d) GO-Fe_3O_4

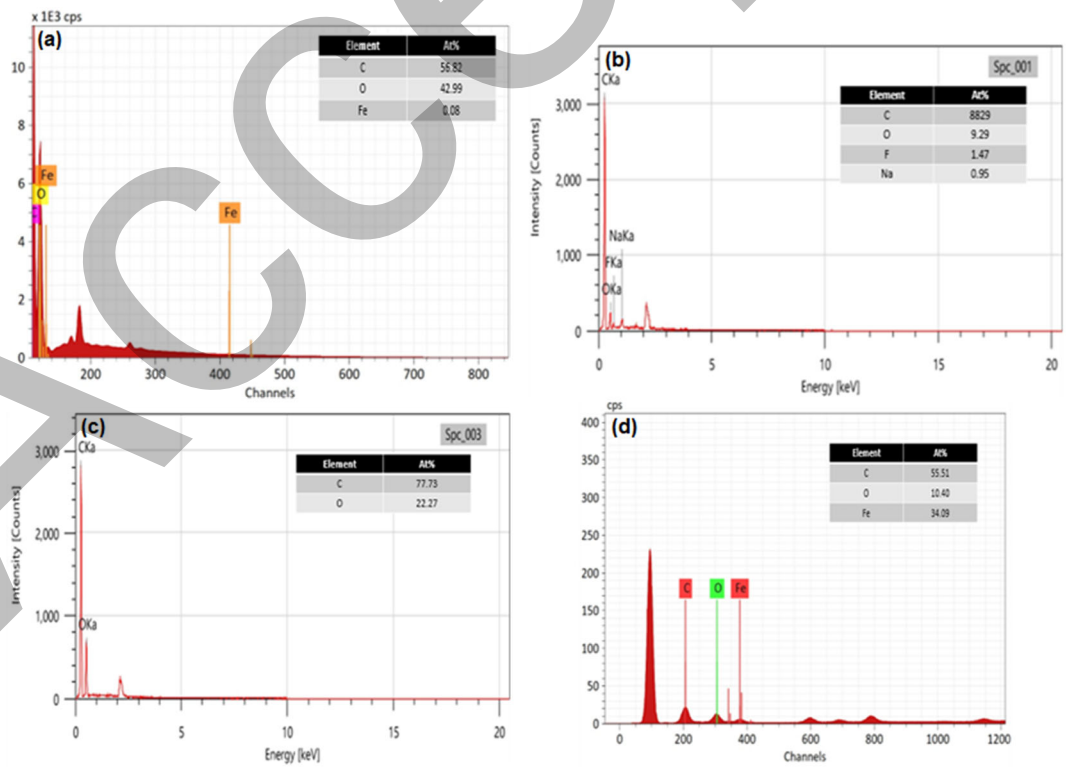

Fig 4. EDS of (a) CSP, (b) graphite, (c) GO, and (d) GO-Fe_3O_4

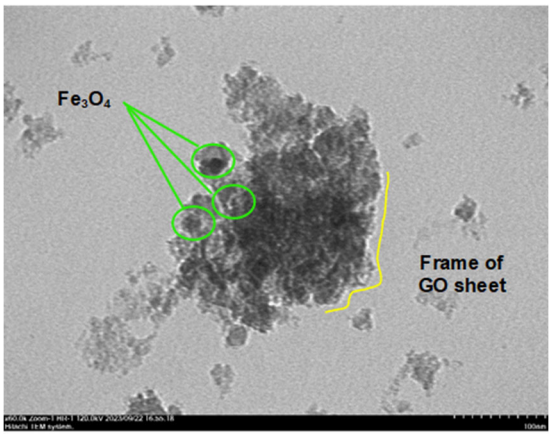

Fig 5. TEM images and particle diameter distribution histogram of the produced GO-Fe_3O_4

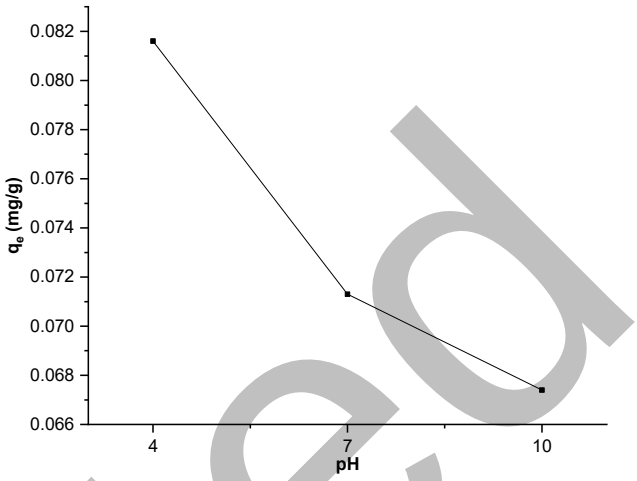

Fig 6. Adsorption of RhB in different pH values

These images show that the surfaces of GO are uniformly coated with black Fe_3O_4 nanoparticles, which are distributed densely. The distribution of these particles is such that there is minimal agglomeration [17].

Adsorption Experiment

The adsorption test was performed based on previous research [21], which has been modified on adsorbents. The test on RhB was carried out at optimum conditions, where a total of 0.5 g adsorbent was added to 10 mL of 4 mg/L RhB. The pH of RhB was adjusted by 0.1 M HNO_3 and 0.1 M NaOH in the range (4, 7, and 10). Adsorption isotherms are evaluated at different concentrations (6, 8, 10, 12, and 14 mg/L). In each adsorption test, the adsorbent was separated with magnets, sonicated for 5 min, and vortexed at 350 rpm. Following these steps, the sample was prepared and analyzed with a UV-vis spectrophotometer at 554 nm. The effectiveness of GO-Fe_3O_4 in removal was demonstrated through the adsorption efficiency, which is quantified in terms of the amount of adsorbate removed per unit mass of adsorbent (q_e, mg/g), as well as the percentage of removal, which is represented by Eq. (2) and (3);

$$R(\%) = \frac{C_0 - C_e}{C_0} \times 100\% \quad (2)$$

$$q_e = \frac{(C_0 - C_e)V}{m} \quad (3)$$

where V represents the volume of dye solution (L), m denotes the mass of GO-Fe_3O_4 (mg), while C_0 and C_e denote the initial and equilibrium concentrations of RhB (mg/L), respectively [34].

Effect of initial pH

Determination of the optimum pH of RhB adsorption using adsorbents of research samples is presented in Fig. 6. The impact of pH on the adsorption of dye was examined over a range of pH values from 4, 7, and 10. Fig. 6 demonstrates that the efficiency of RhB removal gradually declines as the pH rises from 4 to 10. This phenomenon can be attributed to the transformation of RhB from its cationic and monomeric form to a zwitterionic state at lower pH levels, forming larger molecular aggregates. These aggregates hinder the π–π interactions between RhB molecules and GO's aromatic rings [35]. Interestingly, when the pH exceeds 7, a slight increase in removal efficiency is observed, owing to the electrostatic attraction between RhB and the negatively charged GO in alkaline conditions. Despite these variations, the composites maintain satisfactory efficiency for RhB removal across a wide pH spectrum.

Effect of contact time

Fig. 7 shows that the optimum contact duration is 120 min, yielding a q_e of 0.0713 mg/g (89.16%). The adsorption rate experiences a sharp increase during the initial contact period, followed by a gradual deceleration over time until equilibrium adsorption is achieved within the 90–180 min range. The system reaches equilibrium within 30 min. In the early stages (30 min),

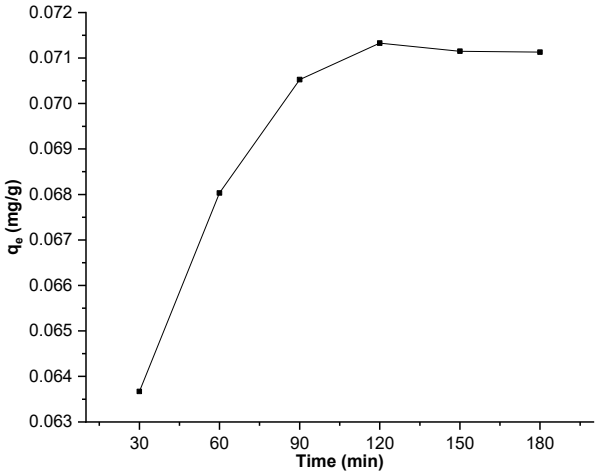

Fig 7. The graph depicts the adsorption capacity versus time of contact of GO-Fe_3O_4

the rapid dye adsorption may be attributed to the abundance of active sites on the GO-Fe_3O_4 surface. The adsorption quantity on the adsorbent rises dramatically and is typically governed by the diffusion process from the bulk solution to the adsorbent surface. During the final phase, the dye adsorption quantity likely becomes an attachment-controlled process due to the diminished availability of sorption sites [36].

Kinetic studies

To investigate the mechanism of RhB adsorption onto the adsorbent, pseudo-first-order (PFO) and pseudo-second-order (PSO) models were utilized to investigate the mechanism of RhB adsorption onto the adsorbent. The linearized forms of these models are expressed using the Eq. (4–5) [37]:

$$\text{Pseudo-first-order: } \log(q_e - q_t) = \log q_e - \frac{k_1}{2.303}t \quad (4)$$

$$\text{Pseudo-second-order: } \frac{t}{q_t} = \frac{1}{k_2 q_e^2} + \frac{1}{q_e} \quad (5)$$

where q_e and q_t represent the amounts of dye adsorbed at equilibrium (mg/g) and at any given time t (mg/g), and k_1 and k_2 denote the adsorption constants of PFO and PSO, respectively.

A linearization plot for RhB adsorption onto GO-Fe_3O_4 nanocomposites is presented in Fig. 8. This graph assesses the adsorption mechanism and investigates how the contact time affects the quantity of RhB adsorbed. The study's experimental findings were analyzed using PFO and PSO kinetics models. The PFO kinetic assumes that adsorption is controlled by diffusion and mass transfer of the adsorbate to the adsorption site of the adsorbent, whereas the PSO kinetic model assumes that adsorption occurs through chemisorption [38].

The PSO kinetics model demonstrated the best fit for the experimental data concerning RhB, as evidenced by the correlation coefficients (R^2) for both models, with the latter achieving an R^2 value of 0.98477. Table 1 shows that the theoretical q_e value ($q_{e,cal}$) derived from the PSO model is closely aligned with the experimental values ($q_{e,exp}$). The adsorption process of RhB onto GO-Fe_3O_4 exhibited a strong correlation with the PSO model, further supporting the notion of adsorption via electrostatic interactions. Under acidic conditions, the

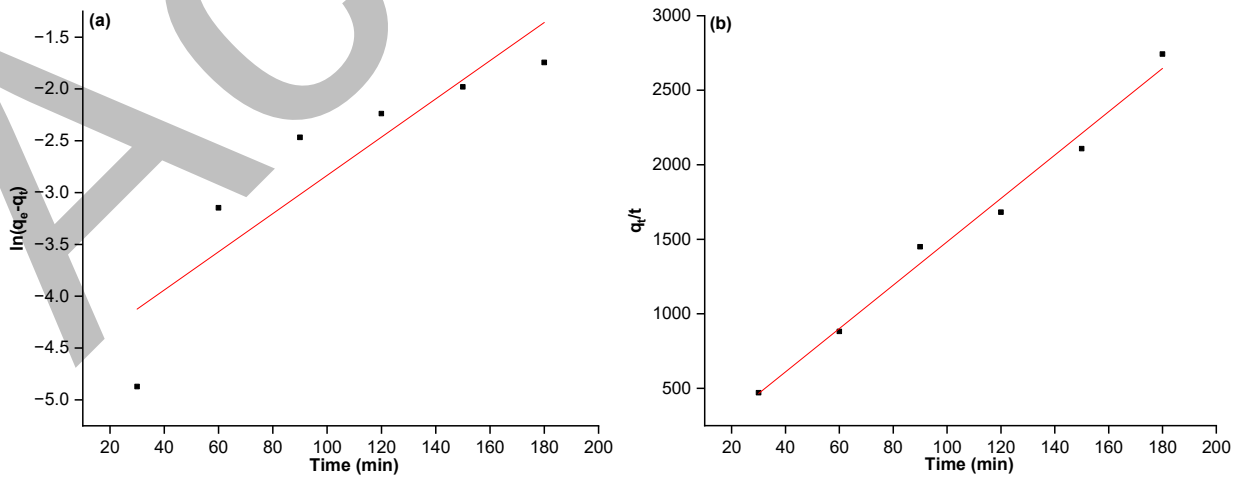

Fig 8. (a) PFO and (b) PSO graph of GO-Fe_3O_4 nanocomposite

Table 1. Parameters of kinetic models for adsorption of RhB to nanocomposites GO-Fe_3O_4

Pseudo-first-order				Pseudo-second-order			
$q_{e,exp}$ (mg/g)	$q_{e,cal}$ (mg/g)	k_1 (min^{-1})	R^2	$q_{e,exp}$ (mg/g)	$q_{e,cal}$ (mg/g)	k_2 (mg/g min)	R^2
0.06803	0.00929	0.00800	0.76390	0.06803	0.06870	0.00016	0.98470

oxygen-containing functional groups (–OH and –COOH) on the GO surface became protonated, resulting in robust electrostatic attractions between the negatively charged RhB molecules and the positively charged adsorbent surfaces. These interactions were primarily facilitated by the positive groups (=$NH^+(C_2H_5)_2$) present in the RhB dye structure.

Effect of initial concentration

The effect of initial concentration is carried out to see the adsorption mechanism on the increase in initial concentration. In Fig. 9, the adsorption capacity increased from 0.1110 to 0.2404 mg/g, while the adsorption percentage of GO-Fe_3O_4 decreased from 92.51 to 85.87% in the increase in the initial concentration of RhB. The adsorption capacity is inversely proportional to the adsorption percentage when the initial concentration increases RhB. This is because the number of molecules of RhB increases with the increase in initial concentration. However, the surface area of GO-Fe_3O_4 is limited, thus increasing the adsorption capacity, but the adsorption percentage is reduced [39]. So, the maximum amount of RhB administered is 0.111 mg/g (92.51%) at a concentration of 6 mg/L.

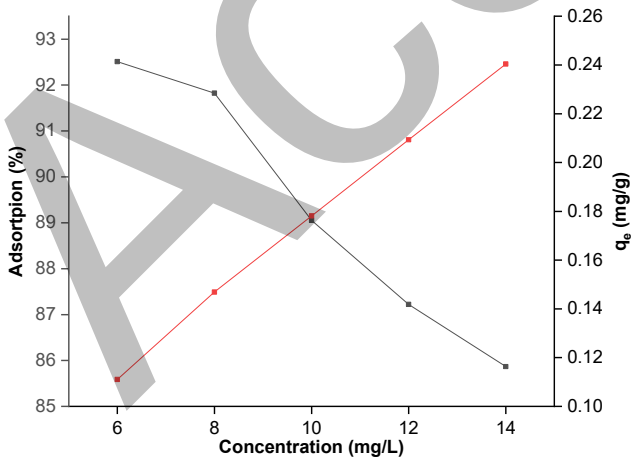

Fig 9. Graph of initial concentration of RhB to %adsorption (black) and adsorption capacity (red) at the optimum time

Isotherm Studies

In order to further investigate the adsorption mechanism of RhB onto GO-Fe_3O_4, the adsorption data were analyzed with the Langmuir, Freundlich, Temkin, and Dubinin-Radushkevich [40] isotherm models. The linearized versions of the models are represented by Eq. (6–9):

Langmuir: $$\frac{C_e}{q_e} = \frac{1}{q_m K_L} + \frac{C_e}{q_m} \quad (6)$$

Freundlich: $$\log q_e = \log K_f \frac{1}{n} \log C_e \quad (7)$$

Temkin: $$q_e = B \ln A + B \ln C_e \quad (8)$$

Dubinin-Radushkevich: $$\ln q_e = \ln q_m - K_{DR}\varepsilon^2 \quad (9)$$

In this framework, C_e and q_e signify the equilibrium concentration of RhB (mg/L) and its adsorption capacity (mg/g), respectively, whilst q_m denotes the maximum adsorption capacity (mg/g). The equilibrium constants for Langmuir (L/mg) and Freundlich ((mg/g) (L/mg)1/n) are represented by K_L and K_f, with n being an empirical constant for the latter. Eq. (5) relates to the Temkin equilibrium binding constant (L/g) and Temkin constant (B), whereas Eq. (6) is associated with K_{DR}, the Dubinin-Radushkevich constant (mol^2/kJ^2), and ε represents the Polanyi potential (J/mol). The calculation of ε utilizes the formula $\varepsilon = RT \ln (1+1/C_e)$, where R stands for the ideal gas constant (J/mol K) and T for the absolute temperature (K). The essential characteristics of the Langmuir isotherm can be examined using the dimensionless constant separation factor R_L ($R_L = 1/(1+K_L C_0)$). The R_L value can indicate whether the adsorption is irreversible ($R_L = 0$), favorable ($0 < R_L < 1$), linear ($R_L = 1$), or unfavorable ($R_L > 1$) [41].

The adsorption isotherm data are shown in Fig. 10, and different parameters are tabulated in Table 2. Table 2 shows that Langmuir isotherms are more suitable for describing the adsorption process, which can be seen from the R^2 value of Langmuir's equation, which is greater than the other equations. Langmuir isotherms

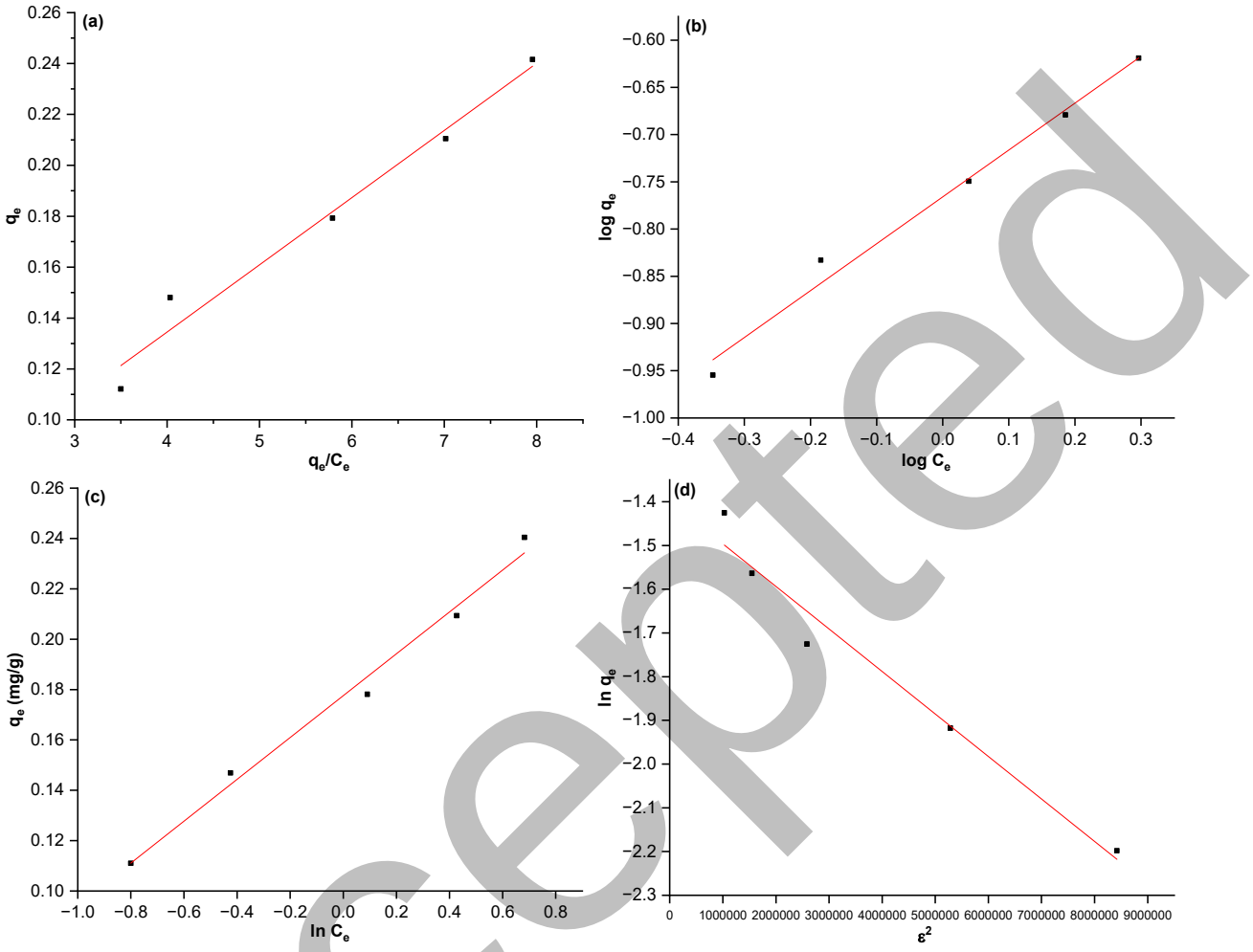

Fig 10. (a) Langmuir, (b) Freundlich, (c) Temkin, and (d) Dubinin-Radushkevich models of RhB sorption

Table 2. Isotherm adsorption of GO-Fe_3O_4

Models	Parameters	Value
Langmuir	R^2	0.9868
	q_m (mg/g)	34.5900
	K_L (L/mg)	1310.2000
	R_L	0.0001
Freundlich	R^2	0.9827
	1/n	0.4961
	K_f (mg/g)(L/mg)	0.1710
Temkin	R^2	0.9842
	B (J/mol)	0.1775
	A (L/g)	2.7182
Dubinin-Radushkevich	R^2	0.9577
	q_m (mg/g)	0.2467

Table 3. Comparison of the maximum adsorption capability of adsorbents in RhB adsorptions

Adsorbents	q_m (mg/g)	Ref.
Fly ash	2.30	[43]
Palm leaves powder	1.42	[44]
Araucaria angustifolia sterile bracts	36.70	[45]
NAOH-treated rice husk	83.00	[46]
Sulfur-doped biochar	33.10	[47]
Fe-N biochar	12.14	[48]
ABL@H_3PO_4	190.63	[49]
Mesoporous palm tree biochar	224.30	[50]
GO-Fe_3O_4	34.59	This work

explain that the RhB adsorption process predominantly occurs between active sites on the adsorbent surface that are spread homogeneously by forming a monolayer. In this study, the R_L value was 0.000127188, which means

that RhB adsorption took place favorably [42]. As summarized in Table 3, the adsorption capacity of GO-Fe_3O_4 for RhB is decent adsorbent. This indicates that the GO-Fe_3O_4 nanocomposite could be an effective material for removing RhB in practical wastewater treatment applications.

■ CONCLUSION

GO-Fe_3O_4 nanocomposites were successfully synthesized using the modified Hummer method and acid treatment for the adsorption of cationic RhB dyes from an aqueous solution. The obtained nanocomposites have been characterized XRD, FTIR, SEM-EDS, and TEM. The optimum adsorption of GO-Fe_3O_4 against RhB occurs at pH 4 with an adsorption capacity of 0.111 mg/g (92.51%), and the optimum initial concentration of 6 mg/L. The Langmuir isotherm model provided the best fit for the equilibrium data when compared to the other models. At room temperature, the Langmuir model calculated the maximum monolayer adsorption capacities of RhB onto GO-Fe_3O_4 nanocomposite to be 34.59 mg/g. The GO-Fe_3O_4 exhibited optimum adsorption of 89.16% for RhB after 2 h. The adsorption mechanism involved electrostatic attraction between the negatively charged GO surface and the protonated RhB molecules. The PSO model best described the adsorption kinetics data for RhB. Furthermore, the magnetic properties of the GO-Fe_3O_4 material make it suitable for practical applications in effectively removing organic azo dyes from wastewater.

■ ACKNOWLEDGMENTS

The researchers would like to extend their appreciation to Sam Ratulangi University for furnishing the necessary materials and laboratory facilities in support of this study.

■ CONFLICT OF INTEREST

The authors state that they possess no financial or personal interests that may have influenced the work presented in this paper.

■ AUTHOR CONTRIBUTIONS

Conceptualization, Henry Fonda Aritonang; methodology, Henry Fonda Aritonang and Alexander Souhuat; sample preparation and data curation, Henry Fonda Aritonang, Alexander Souhuat, and Harry Steven Julius Koleangan; writing-original draft preparation, Henry Fonda Aritonang, Alexander Souhuat, and Harry Steven Julius Koleangan; writing-review and editing, Henry Fonda Aritonang, Alexander Souhuat, Harry Steven Julius Koleangan. All authors have read and agreed to the published version of the manuscript.

■ REFERENCES

[1] Chen, H., Yu, X., Wang, X., He, Y., Zhang, C., Xue, G., Liu, Z., Lao, H., Song, H., Chen, W., Qian, Y., Zhang, A., and Li, X., 2021, Dyeing and finishing wastewater treatment in China: State of the art and perspective, *J. Cleaner Prod.*, 326, 129353.

[2] Yukseler, H., Uzal, N., Sahinkaya, E., Kitis, M., Delik, F.B., and Yetis, U, 2017, Analysis of the best available techniques for wastewaters from a denim manufacturing textile mill, *J. Environ. Manage.*, 203, 1118–1125.

[3] Contreras, M., Grande-Tovar, C.D., Vallejo, W., and Chaves-López, C., 2019, Bio-removal of methylene blue from aqueous solution by *Galactomyces geotrichum* KL20A, *Water*, 11 (2), 282.

[4] Pervez, M.N., and Stylios, G.K., 2018, Investigating the synthesis and characterization of a novel "green" H_2O_2-assisted, water-soluble chitosan/polyvinyl alcohol nanofiber for environmental end uses, *Nanomaterials*, 8 (6), 395.

[5] Sherlala, A.I.A, Raman, A.A.A., Bello, M.M., and Buthiyappan, A., 2019, Adsorption of arsenic using chitosan magnetic graphene oxide nanocomposite, *J. Environ. Manage.*, 246, 547–556.

[6] Albanio, I.I., Muraro, P.C.L., and da Silva, W.L., 2021, Rhodamine B dye adsorption onto biochar from olive biomass waste, *Water, Air, Soil Pollut.*, 232 (5), 214.

[7] da Silva, W.L., Muraro, P.C.L., Pavoski, G., Espinosa, D.C.R., and dos Santos, J.H.Z., 2022, Preparation and characterization of biochar from cement waste for removal of rhodamine B dye, *J. Mater. Cycles Waste Manage.*, 24 (4), 1333–1342.

[8] Sharma, J., Sharma, S., Bhatt, U., and Soni, V., 2022, Toxic effects of rhodamine B on antioxidant system and photosynthesis of *Hydrilla verticillate*, *J. Hazard. Mater. Lett.*, 3, 100069.

[9] Zhou, Y., Li, Z., Ji, L., Wang, Z., Cai, L., Guo, J., Song, W., Wang, Y., and Piotrowski, A.M., 2022, Facile preparation of alveolate biochar derived from seaweed biomass with potential removal performance for cationic dye, *J. Mol. Liq.*, 353, 118623.

[10] Kodama, K., Thao, N.T.T., and Saitoh, T., 2023, Effect of air bubbles on the membrane filtration of rhodamine B, *Anal. Sci*., 39 (9), 1601–1605.

[11] Wei, Z., Kang, X., Xu, S., Zhou, X., Jia, B., and Feng, Q., 2021, Electrochemical oxidation of rhodamine B with cerium and sodium dodecyl benzene sulfonate co-modified Ti/PbO_2 electrodes: Preparation, characterization, optimization, application, *Chin. J. Chem. Eng*., 32, 191–202.

[12] Rahdar, S., Rahdar, A., Zafar, M.N., Shafqat, S.S., and Ahmadi, S., 2019, Synthesis and characterization of MgO supported Fe-Co-Mn nanoparticles with exceptionally high adsorption capacity for rhodamine B dye, *J. Mater. Res. Technol.*, 8 (5), 3800–3810.

[13] Huang, Z., Wang, T., Shen, M., Huang, Z., Chong, Y., and Cui, L., 2019, Coagulation treatment of swine wastewater by the method of *in-situ* forming layered double hydroxides and sludge recycling for preparation of biochar composite catalyst, *Chem. Eng. J*., 369, 784–792.

[14] Nubail, A., Yusmaniar, Y., and Rahman, A., 2019, Adsorpsi pewarna eosin Y menggunakan komposit silika gel termodifikasi 3-aminopropiltrietoksisilan (APTES)-karbon aktif dari bahan alam, *JRSKT*, 8 (2), 1–8.

[15] Tatinting, G.D., Aritonang. H.F., and Wuntu, A.D, 2021, Sintesis nanopartikel Fe_3O_4-polietilen glikol (PEG) 6000 dari pasir besi pantai Hais sebagai adsorben logam kadmium (Cd), *Chem. Prog*., 14 (2), 131–137.

[16] Aritonang, H.F., Onggo, D., Ciptati, C., and Radiman, C.L., 2015, Insertion of platinum particles in bacterial cellulose membranes from $PtCl_4$ and H_2PtCl_6 precursors, *Macromol. Symp*., 353 (1), 55–61.

[17] Oluwasina, O.O., Fahmi, M.Z., and Oluwasina, O.O., 2023, Performance assessment: Influence of sorbate-sorbent interphase using magnetite modified graphene oxide to improve wastewater treatment, *Indones. J. Chem*., 23 (4), 1077–1094.

[18] Heidarizadeh, M., Doustkhah, E., Rostamnia, S., Rezaei, P.F., Harzevili, F.D., and Zeynizadeh, B., 2017, Dithiocarbamate to modify magnetic graphene oxide nanocomposite (Fe3O4-GO): A new strategy for covalent enzyme (lipase) immobilization to fabrication a new nanobiocatalyst for enzymatic hydrolysis of PNPD, *Int. J. Biol. Macromol.*, 101, 696–702.

[19] Al-Ruqeishi, M.S., Mohiuddin, T., Al-Moqbali, M., Al-Shukaili, H., Al-Mamari, S., Al-Rashdi, H., Al-Busaidi, R., Sreepal, V., and Nair, R.R., 2020, Graphene oxide synthesis: Optimizing the Hummers and Marcano methods, *Nanosci. Nanotechnol. Lett*., 12 (1), 88–95.

[20] Kabir Ahmad, R., Anwar Sulaiman, S., Yusup, S., Sham Dol, S., Inayat, M., and Aminu Umar, H., 2021, Exploring the potential of coconut shell biomass for charcoal production, *Ain Shams Eng. J.*, 13 (1), 101499.

[21] Lestari, I., Kurniawan, E., Gusti, D.R., and Yusnelti, Y., 2020, Magnetite Fe_3O_4-activated carbon composite as adsorbent of rhodamine B dye, *IOP Conf. Ser.: Earth Environ. Sci.*, 483 (1), 012046.

[22] Pauner, I.D.M., Senolinggi, G.P., Dullah, F.A., Laseduw, G.P.D., and Aritonang, H.F., 2023, Magnetic nanocomposite-chitosan based on North Sulawesi iron sand as heavy metal adsorbent and synthetic dyes in textile industry waste, *AIP Conf. Proc.*, 2694 (1), 020001.

[23] Directorate General of Estate Crops, 2022, *Statistical of National Leading Estate Crops Commodity 2020-2022*, Ministry of Agriculture Republic of Indonesia, Jakarta, Indonesia.

[24] Fu, R., and Zhu, M., 2016, Synthesis and characterization of structure of Fe_3O_4@graphene

oxide nanocomposite, *Adv. compos. Let*., 25 (6), 143–146.

[25] Tamuntuan, G., Tongkurut, H.J.S., and Pasau, G, 2017, Analisis suseptibilitas dan histeresis magnetik pada endapan pasir besi di Sulawesi Utara, *J. MIPA*, 6 (2), 105–108.

[26] Sujiono, E.H., Zurnansyah, Z., Zabrian, D., Dahlan, M.Y., Amin, B.D., Samnur, S., and Agus, J., 2020, Graphene oxide based coconut shell waste: synthesis by modified Hummers method and characterization, *Heliyon*, 6 (8), e04568.

[27] Sebayang, P., Kurniawan, C., Aryanto, D., Setiadi, E.A., Tamba, K., Djuhana, D., and Sudiro, T, 2018, Preparation of Fe_3O_4/bentonite nanocomposite from natural iron sand by co-precipitation method for adsorbents materials, *IOP Conf. Ser.: Mater. Sci. Eng.*, 316 (1), 012053.

[28] Tanwar, S., and Mathur, D., 2020, Magnetite-graphene oxide nanocomposites: facile synthesis and characterization of optical and magnetic property, *Mater. Today: Proc.*, 30, 17–22.

[29] Jahan, M., and Feni, F., 2022, Environmentally friendly bifunctional catalyst for OOR and OER from coconut shell particles, *Adv. Mater. Phys. Chem.*, 12, 106–123.

[30] Bakti, I.A., and Gareso, P.L., 2018, Characterization of active carbon prepared from coconuts shells using FTIR, XRD and SEM techniques, *JIPF Al-Biruni*, 7 (1), 33–39.

[31] Liu, G., Wang, L., Wang, B., Gao, T., and Wang, D., 2015, A reduced graphene oxide modified metallic cobalt composite with superior electrochemical performance for supercapacitors, *RSC Adv.*, 5 (78), 63553–63560.

[32] Gautam, D., Samal, R.R., Kumar, S., Hooda, S., and Dheer, N., 2023, One pot chemical co-precipitation preparation of magnetic graphene oxide-deltamethrin nanoformulations for management of *Aedes aegypti*, *J. Appl. Nat. Sci.*, 15 (1), 194–202.

[33] Yan, J.C., Zeng, X.Q., Ren, T.H., and van der Heide, E., 2015, Exploring an alternative aqueous lubrication concept for biomedical applications: Hydration lubrication based on O/W emulsions combined with graphene oxide, *Biosurf. Biotribol.*, 1 (2), 113–123.

[34] Abbas, R.F., Hami, H.K., Mahdi, N.I., and Waheb, A.A., 2020, Removal of eriochrome black T dye by using Al_2O_3 nanoparticles: Central composite design, isotherm and error analysis, *Iran. J. Sci. Technol., Trans. A: Sci.*, 44 (4), 993–1000.

[35] Jiang, G., Chang, Q., Yang, F., Hu, X., and Tang, H., 2015, Sono-assisted preparation of magnetic ferroferric oxide/graphene oxide nanoparticles and application on dye removal, *Chin. J. Chem. Eng.*, 23 (5), 510–515.

[36] Nuengmatcha, P., Mahachai, R., and Chanthai, S., 2016, Adsorption capacity of thr as-synthetic graphene oxide for the removal of alizarin red S dye from aqueous solution, *Orient. J. Chem.*, 32 (3), 1399–1410.

[37] Jara, A.D., and Kim, J.Y., 2020, Chemical purification processes of the natural crystalline flake graphite for Li-ion battery anodes, *Mater. Today Commun.*, 25, 101437.

[38] Kırbıyık, Ç. Pütün, A.E., and Pütün, E., 2017, Equilibrium, kinetic, and thermodynamic studies of the adsorption of Fe(III) metal ions and 2,4-dichlorophenoxyacetic acid onto biomass-based activated carbon by $ZnCl_2$ activation, *Surf. Interfaces*, 8, 182–192.

[39] Barale, M., Lefèvre, G., Carrette, F., Catalette, H., Fédoroff, M., and Cote, G., 2008, Effect of the adsorption of lithium and borate species on the zeta potential of particles of cobalt ferrite, nickel ferrite, and magnetite, *J. Colloid Interface Sci.*, 328 (1), 34–40.

[40] Güneş, K., 2023, Isotherm and kinetic modeling of the adsorption of methylene blue, a cationic dye, on pumice, *Int. J. Chem. Technol.*, 7 (1), 67–74.

[41] Chen, L., Li, Y., Du, Q., Wang, Z., Xia, Y., Yedinak, E., Lou, J., and Ci, L., 2017, High performance agar/graphene oxide composite aerogel for methylene blue removal, *Carbohydr. Polym.*, 155, 345–353.

[42] Inyinbor, A.A., Adekola, F.A., and Olatunji, G.A., 2015, Adsorption of rhodamine B dye from

aqueous solution on *Irvingia gabonensis* biomass: Kinetics and thermodynamics studies, *S. Afr. J. Chem*., 68, 115–125.

[43] Kuśmierek, K., Fronczyk, J., and Świątkowski, A., 2023, Adsorptive removal of rhodamine B dye from aqueous solutions using mineral materials as low-cost adsorbents, *Water, Air, Soil Pollut.*, 234 (8), 531.

[44] Khan, M.I., Almanassra, I.W., Shanableh, A., Atieh, M.A., Manzoor, S., Hayat, M., Besbes, M., Elgharbi, S., Alimi, F., and Jemmali, M., 2024, Utilization of palm leaves powder for removal of rhodamine-B from an aqueous solution, *Desalin. Water Treat.*, 317, 100159.

[45] Matias, C.A., de Oliveira, L.J.G.G., Geremias, R., and Stolberg, J., 2020, Biosorption of rhodamine B from aqueous solution using *Araucaria angustifolia* sterile bracts, *Rev. Int. Contam. Ambiental*, 36 (1), 97–104.

[46] Khan, M.I., and Shanableh, A., 2022, Adsorption of rhodamine B from an aqueous solution onto NaOH-treated rice husk, *Desalin. Water Treat.*, 254, 104–115.

[47] Vigneshwaran, S., Sirajudheen, P., Karthikeyan, P., and Meenakshi, S., 2021, Fabrication of sulfur-doped biochar derived from tapioca peel waste with superior adsorption performance for the removal of malachite green and rhodamine B dyes, *Surf. Interfaces*, 23, 100920.

[48] Li, X., Shi, J., and Luo, X., 2022, Enhanced adsorption of rhodamine B from water by Fe-N co-modified biochar: Preparation, performance, mechanism and reusability, *Bioresour. Technol.*, 343, 126103.

[49] Li, P., Zhao, T., Zhao, Z., Tang, H., Feng, W., and Zhang, Z., 2023, Biochar derived from Chinese herb medicine residues for rhodamine B dye adsorption, *ACS Omega*, 8 (5), 4813–4825.

[50] Azeez, L., Adefunke, O., Oyedeji, A.O., Agbaogun, B.K., Busari, H.K., Adejumo, A.L., Agbaje, W.B., Adeleke, A.E., and Samuel, A.O., 2024, Facile removal of rhodamine B and metronidazole with mesoporous biochar prepared from palm tree biomass: Adsorption studies, reusability, and mechanisms, *Water Pract. Technol.*, 19 (3), 730–744.